Check for updates

Reconfigurable nanophotonic silicon probes for sub-millisecond deep-brain optical stimulation

Aseema Mohanty[1,2,7], Qian Li [ID][3,4,7], Mohammad Amin Tadayon[1], Samantha P. Roberts[1], Gaurang R. Bhatt [ID][1], Euijae Shim[1], Xingchen Ji [ID][1,2], Jaime Cardenas [ID][1,5], Steven A. Miller[1], Adam Kepecs [ID][3,4,6 ✉] and Michal Lipson [ID][1 ✉]

The use of nanophotonics to rapidly and precisely reconfigure light beams for the optical stimulation of neurons in vivo has remained elusive. Here we report the design and fabrication of an implantable silicon-based probe that can switch and route multiple optical beams to stimulate identified sets of neurons across cortical layers and simultaneously record the produced spike patterns. Each switch in the device consists of a silicon nitride waveguide structure that can be rapidly (<20 μs) reconfigured by electrically tuning the phase of light. By using an eight-beam probe, we show in anaesthetized mice that small groups of single neurons can be independently stimulated to produce multineuron spike patterns at sub-millisecond precision. We also show that a probe integrating co-fabricated electrical recording sites can simultaneously optically stimulate and electrically measure deep-brain neural activity. The technology is scalable, and it allows for beam focusing and steering and for structured illumination via beam shaping. The high-bandwidth optical-stimulation capacity of the device might facilitate the probing of the spatiotemporal neural codes underlying behaviour.

Nanophotonics, or chip-scale optical systems, provide the ability to rapidly and precisely reconfigure light beams using a compact technology. In the infrared spectral range, nanophotonic devices are widely used in data communications to overcome traditional bandwidth limitations of electrical interconnects[1–4]. In the visible spectral range, nanophotonic devices hold promise for use in biological applications, but these devices have remained technically elusive due to the challenges of reconfiguring and guiding light at these smaller dimensions[5–14]. In neuroscience, for example, there is a need for implantable optical devices to optogenetically stimulate neurons across deep brain regions with speed and precision matching state-of-the-art recording probes[15–25]. Here we demonstrate reconfigurable nanophotonic devices in the visible wavelength range and show its application in vivo in the brain. We demonstrate an implantable silicon-based probe with the ability to rapidly (<20 μs) switch and route multiple optical beams using a nanoscale switching network. Each switch consists of a silicon nitride (SiN) waveguide structure that can be reconfigured by electrically tuning the phase of light and is designed for robustness to fabrication variation, enabling scalable, multifunctional devices. By implanting an eight-beam nanoprobe in mouse visual cortex, we demonstrate in vivo the ability to stimulate identified sets of neurons across layers to produce multineuron spike patterns and record them simultaneously with sub-millisecond temporal precision. Finally, we use a fully integrated four-beam nanoprobe with co-fabricated electrical recording sites to demonstrate the compatibility of nanophotonics with high-density neural recording technologies. This nanophotonic technology can be scaled up, opening the door to implantable probe technologies that are able to simultaneously record and stimulate the activity of large neural populations in deep brain regions with sub-millisecond precision[1,15,16]. Our technology provides building blocks critical to visible nanophotonic systems for three-dimensional beam shaping, enabling structured illumination, focusing and steering in deep brain regions[5]. We expect this technology to enable researchers to test a variety of hypotheses about how spatiotemporal patterns of neural activity underlie behaviour and gain a deeper understanding of the neural code.

Nanophotonic devices are miniaturized and reconfigurable optical circuits with the potential to probe and control biological systems. These optical devices rely on micrometre-scale tunable waveguide elements to control the phase of light and enable switching, steering and shaping of optical beams using interferometric structures[2,5–8,26,27]. As a consequence, nanophotonic devices are fast and low power, in contrast to traditional tabletop optical systems, which rely on moving parts that limit their speed due to their mass and size[28]. Nanophotonic devices can also be markedly scaled up and integrated with electronics to create multifunctional optoelectronic microsystems since they are manufactured using standard nanofabrication techniques used by the electronic complementary metal-oxide-semiconductor (CMOS) industry[1,13]. Nanophotonic modulators, switches and reconfigurable filters have been demonstrated with speeds beyond a gigahertz and up to 1,024 interconnected components, enabling minimal footprint for optical communication transceivers in the near-infrared region[6,29,30]. These optical transceivers have overcome fundamental bandwidth limitations of traditional electrical interconnects, enabling faster data transmission over long distances[1,4]. In addition, these miniaturized optical circuits have enabled development of fields such as integrated quantum optics and optical phased arrays for remote sensing using light detection and ranging[9,31]. However, most reconfigurable nanophotonic devices have been developed for longer wavelengths in the near-infrared spectral range, limiting their applicability in

[1]Department of Electrical Engineering, Columbia University, New York, NY, USA. [2]School of Electrical and Computer Engineering, Cornell University, Ithaca, NY, USA. [3]Cold Spring Harbor Laboratory, Cold Spring Harbor, New York, NY, USA. [4]Department of Neuroscience, Washington University in St. Louis, St. Louis, MO, USA. [5]Institute of Optics, University of Rochester, Rochester, NY, USA. [6]Department of Psychiatry, Washington University in St. Louis, St. Louis, MO, USA. [7]These authors contributed equally: Aseema Mohanty, Qian Li. ✉e-mail: akepecs@wustl.edu; ml3745@columbia.edu
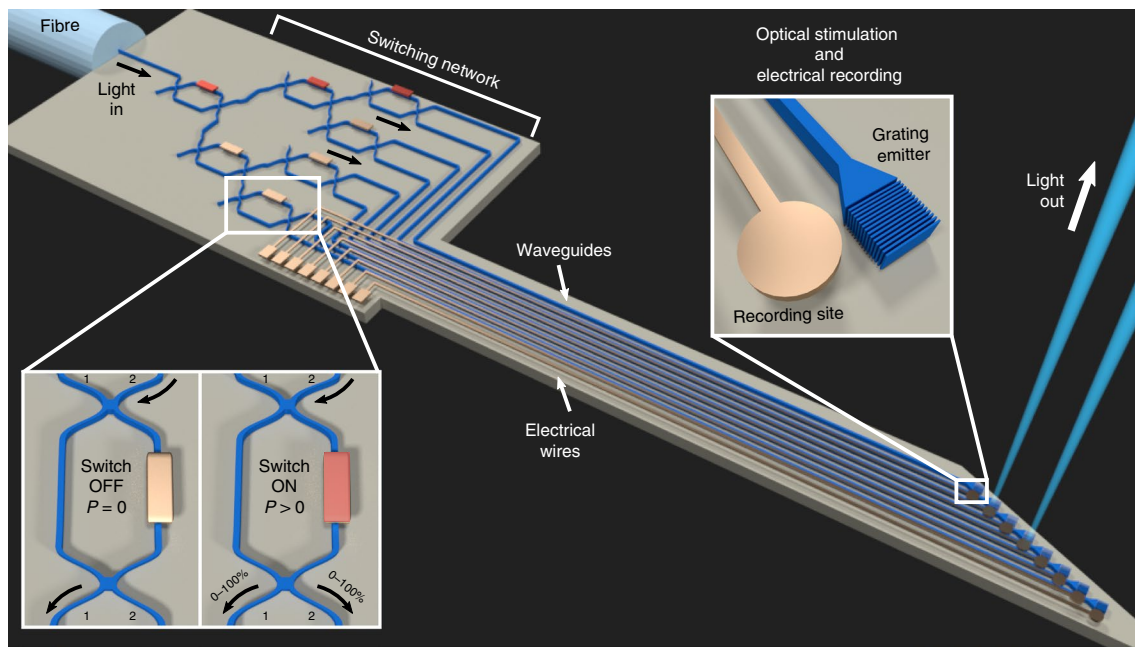
Fig. 1 | Schematic of an implantable probe based on reconfigurable nanophotonics operating in the visible spectral range for optogenetic neuromodulation. The probe forms independently switchable beams within a microsecond time scale. Light is input through a fibre at the top of the device into a single waveguide and is sent to the switching network. The output of the switching network is sent to grating emitters located at the bottom of the probe that send the light outward to excite the neurons. Recording electrode sites are placed near the grating emitter to record nearby neural activity. To minimize electrical interference and heating effects, we use long routing waveguides to place the active photonics that switch the light outside of the brain several millimetres away from the target neural-activation area. Bottom left inset: a single 1×2 MMI-based switch that routes light between two ports. Depending on the electrical power applied to the switch, light can exit any of the two output ports. If light enters the switch through input port 1 (port 2), if no power P is applied ($P = 0$, left) light exits through output port 2 (port 1). As the power on the switch is increased ($P > 0$, right), light is continuously tuned between output port 1 (port 2) and output port 2 (port 1) from 0 to 100%, until all the light is completely in port 2 (port 1). Top right inset: schematic of grating emitter designed to direct light out of plane.

biology, where visible spectral wavelengths (400–700 nm) are typically required (that is, for applications such as neural control, fluorescent probes, spectroscopy and sensing)[32]. This is because of the high susceptibility of nanophotonic structures to fabrication imperfections in this short wavelength range, since the size of imperfections can be on the same order as the size of the optical mode in these high-confinement structures[13,14,33].

In neuroscience, there is a need for an implantable optical-stimulation technology for targeting neurons across deep regions of the brain with the high spatial resolution and sub-millisecond timing precision shown to be critical to understanding neural circuits[21,22]. The compact size of today's implantable electrical recording probes enables observing neural activity from any region of the brain, including deep brain regions, during chronic behavioural experiments in freely moving animals[15]. High-density silicon probes based on CMOS electronic technology can measure the spiking activity of large neural populations at single-neuron resolution with sub-millisecond precision. Electrical recordings have revealed millisecond precision spiking in auditory, somatosensory, and motor systems; however, only perturbation studies, in which neural spikes are induced, can establish whether the information that is available at these time scales is actually used for network function and behaviour[21–25,34–36]. Optogenetic techniques provide this ability to perturb specific neural circuit elements with light[37]. However, an optical technology is still needed for localized and ultrafast stimulation that can be integrated with electrical probes for deep-brain accessibility. Micrometre-scale light-emitting diodes (micro-LEDs) have been fabricated alongside integrated electrical probes, but they have limited spatial (>100 μm) resolution due to their incoherent Lambertian emission and limited temporal resolution (<30 Hz)

due to heating and electrical interference effects[18–20]. Passive, implantable nanophotonic probes have been demonstrated that do not introduce these undesirable effects; however, they rely on external tabletop optics for reconfiguration that limit the number of controllable optical-stimulation sites and their chronic implantation[10–12,17,38–40]. Miniaturized lasers can also be integrated with nanophotonic waveguides; however, their assembly, size and power dissipation limit the number that can be realized on a single probe[41]. The ability to reconfigure nanophotonic devices would enable light input from a single laser to be distributed to many highly localized emitters to create high-resolution spatiotemporal optical patterns without introducing heating and electrical artefact effects.

To meet this demand, we demonstrate scalable building blocks for enabling microsecond reconfigurable nanophotonic systems in the visible spectral range (at 473 nm) that overcome the typically low fabrication tolerances of nanophotonic devices operating in this spectral range. Furthermore, we show that this technology can be integrated with current recording electrode technology to provide simultaneous simulation and recording of neural activity. The technology is based on waveguides (200 nm by 350 nm cross section) defined in SiN, a material that is transparent in the visible range[42]. These high-confinement waveguides ensure high dispersion and thus high sensitivity and fast response times to small changes in material index with low bending losses. These waveguide characteristics facilitate design of scalable, multifunctional devices that are reconfigurable and miniaturized. Because SiN can be fabricated using standard deposition and etching processes that are CMOS compatible, it allows nanophotonic systems to be fabricated alongside high-density electrical recording site arrays on silicon substrates that can be thinned to <20 μm. To enable visible photonic systems
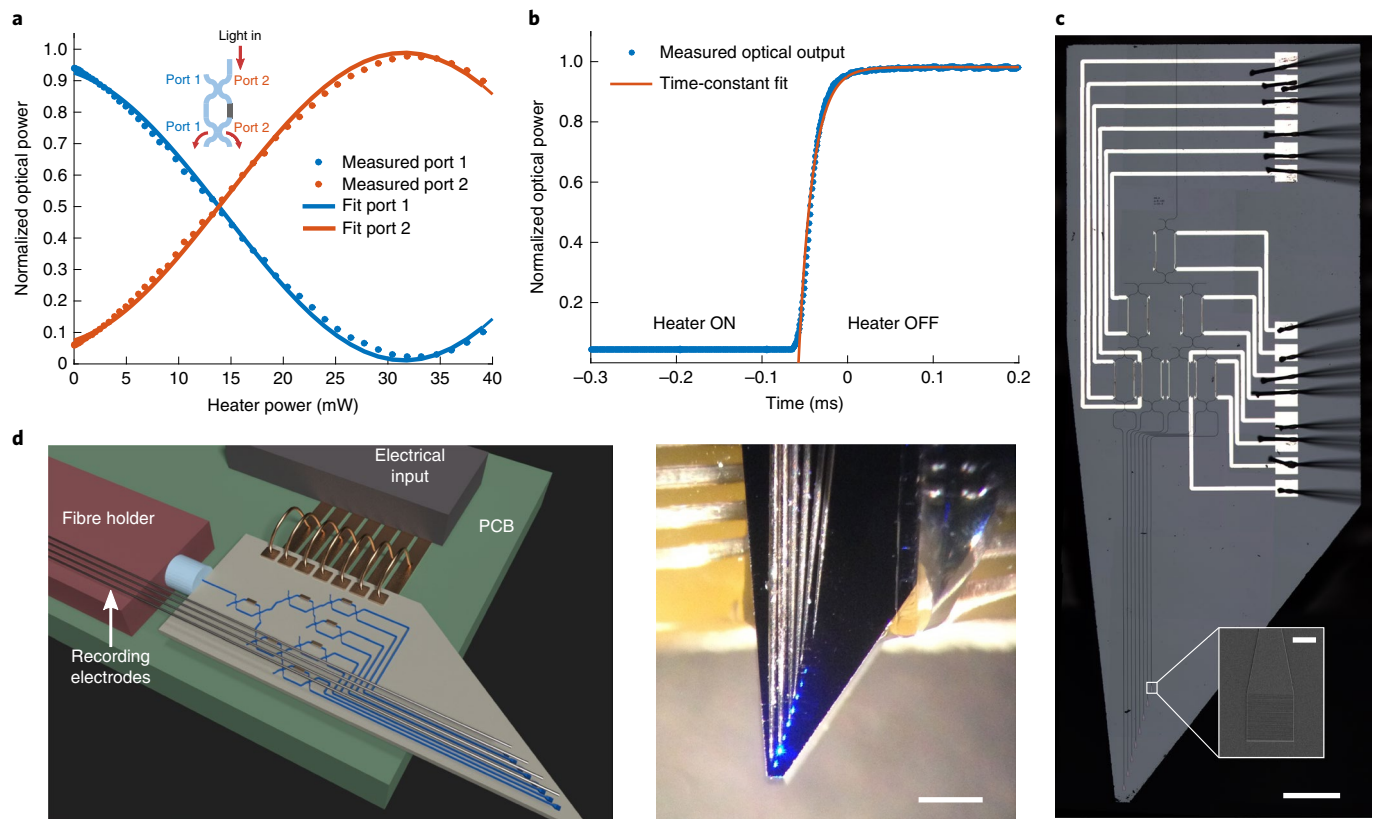
Fig. 2 | Nanophotonic switch operating in the visible spectral range with high extinction ratio and short switching time. a, Normalized optical output power measured through output port 1 and output port 2 of the MZI switch, when 473 nm light is input through input port 2. For a single switch, the measured switch power for full conversion from output port 1 to output port 2 is 30 mW and the ON:OFF contrast ratio is 50:1 (or 17 dB extinction). **b**, Response time of output port 1 switching on when the heater is turned off. The switching time is 20 μs, which we calculate by fitting an exponential to the measured optical output. **c**, Microscope image of the fabricated chip (scale bar (main image), 500 μm). Inset: scanning electron microscope image of the grating emitter (scale bar, 10 μm). **d**, Left: the schematic shows the fibre and electrical packaging on a printed circuit board (PCB) of the neural probe. Right: microscope image of the packaged device with electrodes aligned near the emitters (around 20 μm) and optical output. Scale bar, 500 μm.

that are reconfigurable, we design interferometric switches as the basic building blocks for routing light on a chip (see Fig. 1). These 1×2 (one input and two output) switches can be cascaded so that light from a single laser can be routed to 2^n output grating emitters. To induce robustness to fabrication variation, we design switches based on multimode interferometer (MMI) structures for splitting the light within the interferometer. These switches, due to their dimensional insensitivity, are more robust than traditional directional coupler-based interferometers[43,44] (see inset of Fig. 1 and Supplementary Fig. 1). For reconfiguration, the switches are based on waveguides that are co-fabricated with highly localized microheaters that induce a small local temperature change (ΔT), which in turn induces a refractive index change (Δn) in the SiN waveguide ($\frac{\Delta n}{\Delta T} \approx 4 \times 10^{-5} \mathrm{K}^{-1}$). An induced refractive index change (that is phase change) to one of the interferometer arms determines the spatial interference pattern at the switch output when the two arms are combined. Depending on the electrical power applied to this analogue switch, light can exit either of the two output ports. To fabricate these structures, we use our recently demonstrated high confinement SiN photonic technology with ultra-low loss in the near-infrared spectral range[42]. The fabrication process of the nanophotonic device and its monolithic integration with recording electrodes is described in detail in the Methods and Supplementary Fig. 2.

Results

To characterize the ultimate spatial resolution and speed of our technology, we measure the extinction ratio and switching time

of a single fabricated switch. We show that the measured extinction ratio, or the on/off contrast ratio, between the two outputs of the switch is high, about 50:1 or 17 dB (see Fig. 2a and Methods). This is similar to the extinction ratio achieved in more traditional devices operating at near-infrared wavelengths[29]. This high extinction ratio enables full control over the path of light to allow independent control of output beams even for closely spaced emitters (<1 μm apart). The resulting high spatial resolution of stimulation is important to selectively activate individual neurons. The switching power—the power required to switch the light completely from port 1 to port 2—is approximately 30 mW. We also show fast switching time scales, on the order of 20 μs, well below the typical neural activity time scales that will enable advanced switching schemes in larger nanophotonic systems. We measure the time that it takes to switch the optical state of port 1 as the heater switch is turned off, and the light switches from output port 2 to output port 1 (see Fig. 2b and Methods). These switches can be used as a building block for larger nanophotonic systems with the same high spatial resolution and speed.

To illustrate the power of this technology, we built an implantable nanophotonic probe with eight independently switchable beams with microsecond reconfiguration times. Nanophotonics enables one to control the flow of light dynamically using a network of switches and direct light out of plane as narrow beams using grating emitters, which are located at a distance from the switching network. By cascading multiple 1×2 Mach–Zehnder interference (MZI) switches, we create an eight-beam probe using a 1×8 switching
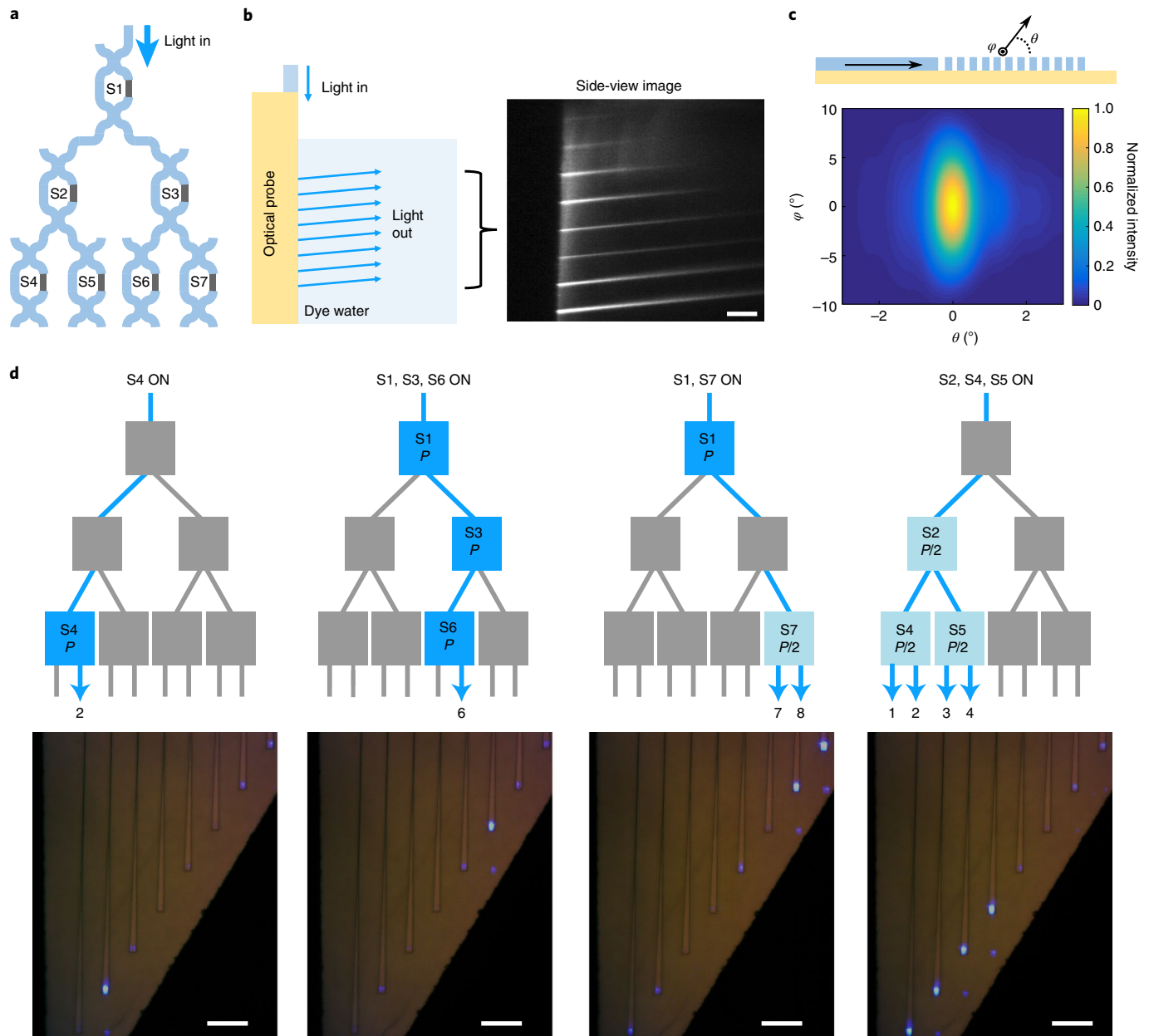
Fig. 3 | Spatial optical patterns generated by the probe to demonstrate dynamic reconfiguration of highly collimated beams. a, Schematic of the optical switch network. Each switch is denoted S*x*, with *x* being its number. **b**, Left: schematic of setup to image the spatial distribution of light output from the nanophotonic probe in fluorescent dye from the side. Right: side view of the grating emitters with 473 nm blue light transmitting through Alexa Fluor 488 dye. Scale bar, 125 μm. **c**, Far-field plot of beam from the grating emitter. The beam emits at a −7° angle, and θ and φ correspond to the axes perpendicular to the direction of propagation of light in the grating emitter as shown in the schematic. **d**, Examples of different switch configurations that produce different optical patterns. Scale bar, 125 μm. Light enters the switch network through the top and exits as indicated by the arrows. Switches indicated by a grey box are OFF and switches indicated by a blue box are ON. *P* indicates full power and *P/2* indicates half the power. The numbers below the arrows at the switch output correspond to the emitter output that is ON. The microscope images below show corresponding emitter configurations of the working device.

network in which the waveguides lead to eight grating emitters. Figure 1 shows the schematic of the implantable probe based on the high-confinement SiN waveguide structures designed for optogenetic excitation in the blue wavelength range (centred at 473 nm) and micrometre-scale electrical recording sites for readout of neural activity (see Methods). Figure 2c shows a microscope image and scanning electron microscope (SEM) image of the fabricated and packaged device. Light is launched into the probe through an optical fibre at the top, coupled into a single waveguide, and then routed through the switching network. The output of the switching

network is sent to grating emitters located at the bottom of the probe that send the light outward to excite the neurons. Using long routing waveguides, we place the active photonics that switches outside of the brain, several millimetres away from the target neural activation area, to minimize interference or heating effects. Note that the gratings can be designed to emit beams at different angles and with different amplitude and phase distributions for controlling the degree of collimation and beam shape. Here we design the gratings to emit light beams perpendicular to the probe, with minimal divergence. We chose the grating size to be 20 μm × 20 μm

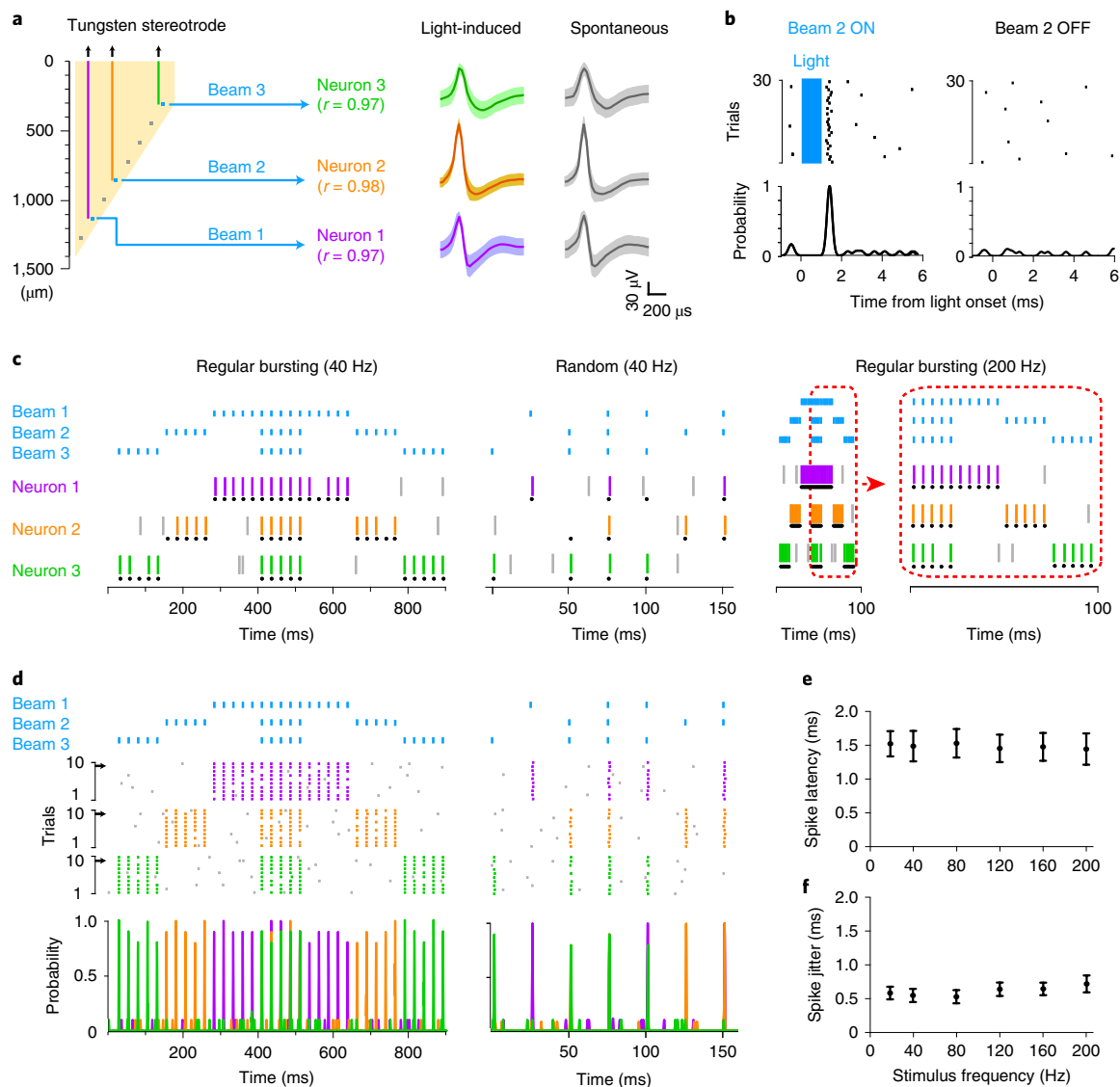**Fig. 4 | In vivo demonstration of a nanoprobe driving multiple individual neurons with precisely timed spike patterns. a**, Schematic of the eight-beam probe for fast, independent control of activity of three ChETA-expressing Gad2 interneurons across layers 2–6 of the V1 and the hippocampus in anaesthetized mice. Three pairs of electrical recording stereotrodes (coloured lines) are positioned next to beam 1–3 (blue squares), respectively. The scale bar shown on the left indicates the insertion depth from brain surface. From each recording site, a single ChETA-expressing Gad2 interneuron (neuron 1–3) is confirmed by evaluating the spike waveform similarity (r) of light-induced spikes (averaged spike waveform in coloured bold line, superimposed with colour-shaded s.d. of spikes) and spontaneous spikes (averaged spike waveform in grey bold line, superimposed with grey-shaded s.d. of spikes). **b**, Representative spike raster and peri-stimulus time histogram of neuron 2 when beam 2 is ON and OFF. Blue line indicates 1 ms light pulse and pulse onset is set to time 0. Probability indicates probability of spiking. **c**, Spike raster of neuron 1–3 driven by series of light pulses delivered in three patterns: (1) regular bursting sequence at 40 Hz, (2) random sequence with highest frequency at 40 Hz, and (3) regular bursting sequence at 200 Hz. Blue line indicates light pulse. For each neuron, coloured line indicates light-induced spike, grey line indicates spontaneous spikes and black dot indicates the timestamp when light-induced spike are supposed to occur. **d**, Representative 10 trials of spike raster and peri-stimulus time histogram of neuron 1–3 in response to repeated regular bursting (left) and random (right) light stimulation at 40 Hz. Bin size, 100 μs. Black arrows point to the specific trial shown in **c**. **e,f**, Summary of spike latency (**e**) and spike jitter (**f**), referring to light onset throughout multiple stimulation frequencies (mean ± s.d., $n = 13$, sorted neurons from 4 mice).

to approximately match the size and density of a network of neurons (see Methods).

We show the ability of this technology to form dynamically reconfigurable optical patterns of highly collimated beams. Figure 3 shows reconfigurable light patterns obtained by applying different power configurations to the switching network. We show that the grating emitters produce low-divergence beams by imaging the probe from the side as it excites a fluorescent dye (see Fig. 3b,c and Methods). Supplementary Discussion 1 discusses the full characterization of the optical crosstalk and loss within the 1×8 switching network.

On the basis of the near-field imaging of the aperture of the grating emitter, we measure the divergence angle to be 2.2° transverse to the waveguide propagation and 3.75° along the waveguide propagation. Supplementary Video 1 shows the eight spots being illuminated independently with low crosstalk. The output optical power density is 15 mW mm⁻², which exceeds the optical intensity threshold for optogenetic neural excitation and, in previous studies[18], ranges from 0.4 mW mm⁻² to 10 mW mm⁻².

The nanophotonic probe enabled us to activate individual neurons with sub-millisecond precision in vivo. Figure 4 shows
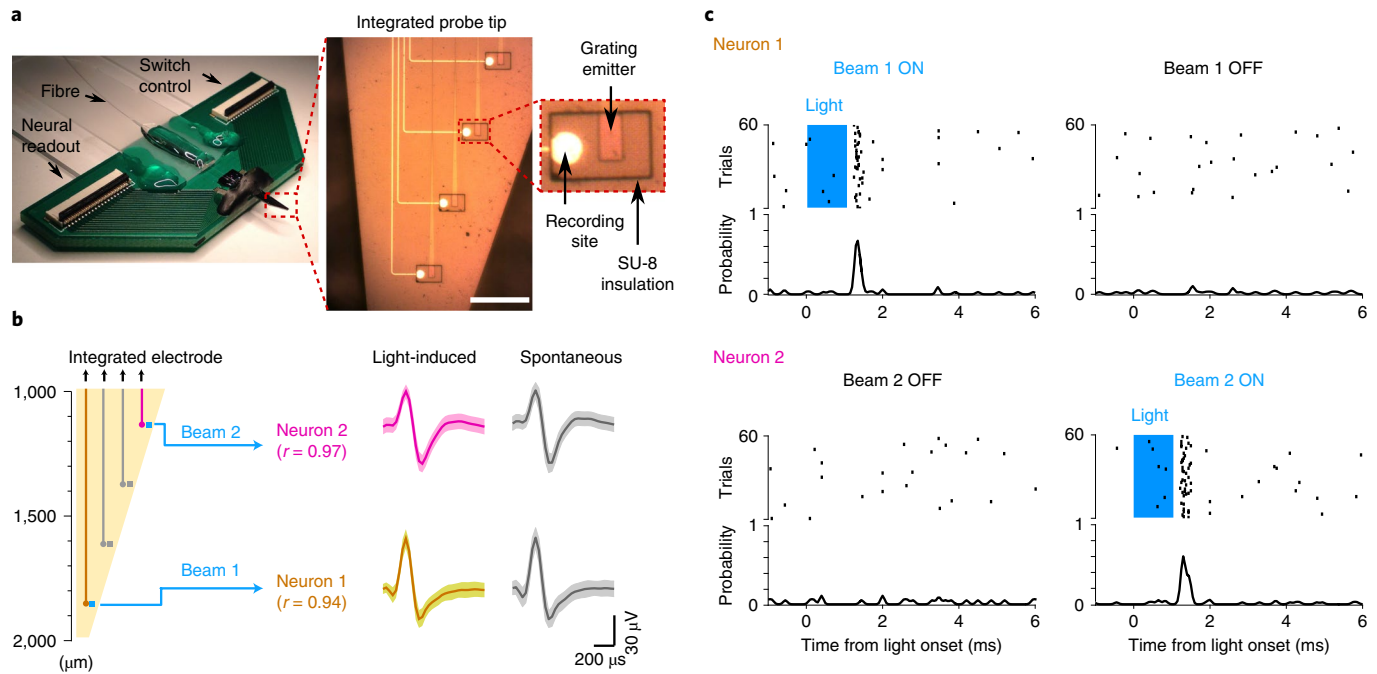
Fig. 5 | In vivo demonstration of a fully integrated nanophotonic probe with Pt recording sites. a, Image of the packaged nanophotonic probe. Inset: microscope image of the inserted tip of the integrated four-beam nanophotonic probe. Pt recording sites are fabricated within 20 μm of each beam, and Pt wires are insulated with SU-8 polymer. Scale bar, 250 μm. **b**, Left: schematic of integrated four-beam nanophotonic probe for independent control of activity of two ChETA-expressing Gad2 interneurons in anaesthetized mice. The scale bar shown on the left indicates the insertion depth from brain surface. Beam 1 and beam 2 (blue squares) are switched to activate neuron 1 and 2, respectively. Two colour-coded lines indicate the integrated electrodes from which we record neuron 1 and 2. Right: spike similarity is confirmed by evaluating the spike waveform similarity (*r*) of light-induced spikes (averaged spike waveform in coloured bold line, superimposed with colour-shaded s.d. of spikes) and spontaneous spikes (averaged spike waveform in grey bold line, superimposed with grey-shaded s.d. of spikes). **c**, Representative spike raster and peri-stimulus time histogram of neuron 1 and 2 when light beam 1 and 2 are ON and OFF. Blue line indicates 1 ms light pulse and pulse onset is set to time 0. Probability indicates probability of spiking.

examples of electrically recorded signals from optically activated neurons across multiple brain regions. Neural activity was recorded with an array of tungsten electrodes aligned to the grating emitters of a nanophotonic probe inserted into the primary visual cortex (V1) and the hippocampus of anaesthetized mice (see Fig. 4a, Supplementary Fig. 4 and Methods). We rendered inhibitory neurons light-activatable by injecting an adeno-associated virus delivering a channelrhodopsin-2 variant (AAV-EF1a-DIO-ChETA-eYFP) in transgenic knock-in mice (Gad2-IRES-Cre). We used this mouse line because Gad2 inhibitory neurons locally inhibit other neurons, minimizing secondary light activation of neurons not expressing the light-sensitive opsin. We used ChETA, a channelrhodopsin-2 variant, because it enables ultrafast optogenetic control[45]. The process for identifying light-tagged Gad2 inhibitory neurons by their significant short-latency light response is described in Methods, 'Stimulus-associated spike latency test', and we also confirmed that we recorded well-isolated single units. Figure 4a shows that light-induced and spontaneously occurring spikes exhibited similar spike waveforms (spike waveform similarity, *r* > 0.95, defined in Methods), as expected from single-neuron signals. Alignment to the 1 ms light pulse revealed low-latency and low-jitter spikes (Fig. 4b). Increasing light intensity above the threshold did not yield additional spikes due to secondary activation by other neurons. On the basis of the low latency and jitter of spikes, and because we targeted inhibitory neurons, these responses are from directly light-activated neurons. We estimated that approximately 1–2 inhibitory neurons can be activated within a 100 μm beam path (the approximately relevant radius for electrical recordings), on the basis of the estimated optical volume and neuron density. We found that an individual light beam activated at most one neuron, and we occasionally co-recorded

putative pyramidal neurons with short-latency troughs in their cross-correlograms, indicative of monosynaptic inhibition from the recorded Gad2 interneuron (Supplementary Fig. 5). These results confirm the ability of the probes to activate individual neurons as observed by recordings from these activated neurons.

Using the eight-beam nanophotonic probe, we generated precisely timed multineuron spike patterns in vivo. Figure 4c,d shows the generation of different spatiotemporal neural patterns, including sequential bursts, random pulses and high-frequency patterns (up to 200 Hz). Figure 4c shows a representative trial of the recorded neural-spike patterns that follow the optical command patterns produced by the beams (blue ticks). These patterns could be evoked with high reliability across neurons and multiple trials (Fig. 4d). We quantified reliability by computing the probability of light-induced spike responses (peri-stimulus time histogram (PSTH)), revealing greater than 90% fidelity across all these patterns. Supplementary Fig. 6 shows additional measurements of two neurons switched at multiple frequencies. The spike latency and jitter of light-induced spikes across repeated patterns were consistently low for stimulation frequencies up to 200 Hz (Fig. 4e,f; *n* = 13 neurons from 4 mice). The high-speed and reliable switching in these experiments demonstrate that our nanophotonic probe can be used in vivo to drive precise and high fidelity population spike patterns.

To demonstrate the technology's compatibility with high-density neural recording technologies, we also fabricated and tested in vivo a fully integrated four-beam nanoprobe with co-fabricated electrical recording sites. We use this fully integrated probe to simultaneously stimulate and record neural activity in deep brain areas of an anaesthetized mouse. Figure 5 shows a four-channel integrated nanophotonic probe with co-fabricated electrodes and emitters side by

side, which we use to independently activate two spatially separated neurons and record spike signals from each of them. We acquired low-noise continuous neural activity from platinum (Pt) recording sites with signal-to noise ratios at 4.73 ± 1.15 (mean $\pm$ s.d.; Supplementary Fig. 8a). This recording quality enabled us to sort uniform spike events from single neurons (spike waveform similarity between light-induced and spontaneous spikes: $r = 0.94$ (neuron 1), $r = 0.97$ (neuron 2); see Fig. 5b). By electrically programming the four-channel switch network, we showed that neuron 1 and neuron 2 were preferentially excited by beam 1 and beam 2, respectively (see Supplementary Fig. 8b). The peri-stimulus time histogram indicated that fast, sustained increase in spike firing only occurred when the proximal beam was switched on (Fig. 5c). Both neurons exhibited light-induced spikes with low latency (neuron 1, 1.38 ms and neuron 2, 1.34 ms) and low jitter (neuron 1, 0.42 ms and neuron 2, 0.48 ms).

Discussion

The technology presented here enables scalability in the number of emitters by leveraging the high power handling of SiN and previously demonstrated techniques for realizing ultra-low-power switches[26,46,47] (see Supplementary Fig. 10 and Supplementary Discussion 2). To further reduce the footprint of emitters along the inserted probe, many optical channels can be directed to a single waveguide using different degrees of freedom of light (that is, wavelength or transverse spatial mode) to control multiple emitters[4] (see Supplementary Fig. 11 and Supplementary Discussion 3). Finally, leveraging previously demonstrated designs of broadband photonic devices to cover the entire range of opsin peak excitation wavelengths (470–600 nm) would enable multicolour experiments involving optical activation and inhibition and targeting multiple neuron types simultaneously[32,48,49]. The nanophotonic waveguides are also compatible with multiphoton optical approaches due to their high power-handling capabilities and moderate nonlinearities in the near-infrared wavelengths, enabling further reach for deep brain stimulation[21,50–54].

The visible-wavelength range nanophotonic switch can be used as a fundamental building block for larger, multifunctional nanophotonic systems and probes. By placing phase-controlled emitters in an array, a tunable optical aperture similar to a reconfigurable lens or spatial light modulator can be implanted in the brain. Optical phased arrays based on arrays of grating emitters controlled by nanophotonic switches in the near-infrared-wavelength range have been used to create steerable and focused beams[5–7]. We show numerical simulations of steered and focused beams using an array of 32 grating emitters in the visible-wavelength range (Supplementary Fig. 12). This same technology can be extended to create arbitrary three-dimensional patterns of optical stimulation[5,27] for structured-illumination imaging techniques (for example, light-sheet and light-field microscopy)[55,56].

Outlook. Our demonstration of a reconfigurable visible-wavelength nanophotonic technology is a step towards implantable optical probes with rapid control over arbitrary populations of single neurons for brain stimulation for neuroscience research. Furthermore, the integration of silicon photonics and electronics will enable integrated probes with optical-stimulation capacity that match the scale and resolution of currently available electrical recording probes[1,12,15]. The development of such multifunctional large-scale devices will enable control over arbitrary, genetically or functionally defined neural populations to study the contribution of precisely timed multineuron patterns to neural computation and behaviour.

Methods

Device design. Here we outline the details of the nanophotonic probe design from input fibre to output grating emitters following Fig. 1, from top to bottom. For fibre-to-chip coupling, we use a horn taper at the input to match the optical mode of a cleaved single mode fibre (Thorlabs 460B). Next, the switching network for

the 1×8 nanophotonic probe consists of seven thermally-tuned MZI switches (see Supplementary Fig. 1 for more details on the switch design). We use EigenMode Expansion (Fimmwave) to numerically simulate the optical properties of the MZI switch and optimize the design for fabrication, wavelength and polarization insensitivity. Each MZI is composed of a 300-μm-long platinum microheater for phase control and two MMI beamsplitters for interference. The waveguides throughout the switching network are based on waveguides with a cross-section 200 nm high and 350 nm wide. We chose this cross-section to minimize losses due to sidewall roughness while remaining near the second-order mode cut-off at 473 nm. The routing waveguides from the switching network are adiabatically tapered to 700 nm for the millimetre-long routing waveguides and then to 20 μm at the grating emitters. We use fully etched grating emitters that are designed to emit beams at near 90° angles from the surface. We use a grating pitch of 260 nm with a 50:50 duty cycle. The grating emitters span about 1 mm and are spaced 80 μm horizontally and 125 μm vertically. For the fully integrated probe, we design low impedance platinum recording electrode sites that have an impedance of 1.2 MΩ that are positioned 20 μm away from each grating emitter.

Device fabrication and packaging. To fabricate the implantable nanophotonic probe, we deposit 200 nm of low-pressure chemical vapour deposition (lpcvd) SiN on a silicon wafer with 5 μm of lpcvd silicon dioxide. Next, we pattern the waveguides using electron beam lithography and a fluorine-based etch. We cover the waveguides with 660 nm of lpcvd high temperature oxide. Next, to pattern the switch and recording electrodes above the waveguide, we use a metal lift-off process to pattern 100 nm of platinum with a titanium adhesion layer and 600 nm of aluminium with a titanium adhesion layer. We pattern a 6 μm SU-8 layer for electrical insulation of the recording electrode wires, leaving the recording sites exposed. We dice the chip at an angle, so that the inserted tip is less than 100 μm. Finally, the silicon substrate below the inserted tip is thinned below 250 μm using a partially masked Bosch etch process. The final tip dimensions are approximately $250 \, \mu m \times 100 \, \mu m$. The probe chip is wire-bonded to a PCB for controlling the switch and recording electrode output, and a fibre is aligned to the chip and attached using UV-curable optical adhesives. For in vivo measurements without integrated electrodes, an array of tungsten electrodes (1 MΩ, 81 μm shaft diameter, 2–3 μm tip diameter; TM33C10 World Precision Instruments) are aligned near the grating emitters and attached to the probe using permanent adhesive. We align the tungsten electrode tip around 20 μm away from the grating emitters. These steps are outlined in detail in Supplementary Fig. 2.

Device characterization. To deliver light to the probe, we use a cleaved single-mode fibre (Thorlabs 460B) to input light from a blue diode laser centred at 473 nm (Model SSL-473-0300-10TM-D-LED, Shanghai Sanctity Laser Technology). For electrical input to the switch, we use a multichannel digital-to-analogue converter module (NI-DAQ) with an amplified output. For the extinction ratio measurement, we use a Newport detector (818-SL), and for the measurement of the time transient, we use a biased silicon detector with 1 ns rise time (DET10A). We take images and video of the switching patterns using a Thorlabs CMOS camera. To image the beams from the side to characterize the beam profile, we insert the device in a small glass container filled with fluorescent dye (Alexa Fluor 488, 32 μM solution) and image using a camera (JVC TK-S241U). To characterize the optical crosstalk across the entire eight-beam probe, we take images of the probe as each channel is independently turned on and integrate pixel values across the grating emitter to acquire the total optical power output of each beam.

To measure the temperature crosstalk on the probe, we measure the change in resistivity of the platinum microheater in switch 5 when its neighbouring switch 4 (200 μm away) is ON. We calibrate the temperature coefficient of resistance (α) of our platinum film by measuring the change in resistance of a switch in a vacuum chamber on a calibrated heated substrate. The temperature is related to the resistivity of the Pt by the following equation: $R = R_0 (1 + \alpha (T - T_0))$, where T is the temperature, T_0 is the reference temperature, R is the resistance at T, and R_0 is the resistance at T_0. For our Pt film, we measure α at $0.00233 \pm 0.00005 \, \mathrm{K}^{-1}$.

Animals. Adult (six-to-eight months old) male or female Gad2-IRES-Cre knock-in mice (Jackson Labs, 010802) were used under the protocol approved by Cold Spring Harbor Laboratory Institutional Animal Care and Use Committee in accordance with National Institutes of Health regulations. Mice were maintained with a reverse 12 h:12 h light:dark cycle with ad libitum food and water.

Virus injection. Gad2-IRES-Cre knock-in mice were anaesthetized with ketamine (100 mg kg^{-1}) and xylazine (10 mg kg^{-1}) mixture by intraperitoneal injection and placed into a stereotactic frame (SR-6M-HT, Narishige). A sagittal incision along the midline was made to expose the cranium, and a craniotomy was made over the target area, the V1 (anterior-posterior, AP: −2.6 mm, medial-lateral, ML: 2.4 mm). Cre-dependent AAV9-EF1a-DIO-ChETA-eYFP vector (1.5 μl; a ChR2 variant from UNC vector core, high-frequency stimulation drivable), was loaded into a glass micropipette (tip diameter ~20 μm) attached to a syringe and was injected into V1 and below in hippocampus at six depths (dorsal-ventral, DV: 0.2, 0.4, 0.8, 1.3, 1.6 and 2.0 mm from the brain surface, 0.25 μl per site, viral titre: 8×10^{12} viral genomes per ml). After each injection, the micropipette was left in place for 5 min

before it was retracted to a higher position. The scalp incision was sutured. The mouse was maintained under a 37 °C heater and under observation until recovery from the anaesthesia, before returning to standard cages. Mice were maintained for four weeks before performing electrophysiological experiments. The delivery of large volume of AAV and the long waiting time for viral expression increased the efficacy and reduced the variability of ChETA expression.

In vivo experiments. For acute in vivo experiments, mice were anaesthetized with dexmedetomidine ($0.25\,mg\,kg^{-1}$, intraperitoneal injection) and placed in the same stereotactic frame as described for virus injection. The craniotomy for virus injection was exposed again and enlarged to a $2 \times 2\,mm^2$. The dura was carefully removed and the probe was inserted slowly using a motorized arm (Thorlabs MTS50-Z8). For testing the eight-beam probe aligned with an array of tungsten stereotrodes, we targeted viral infected areas crossing layers 2–6 of the V1 and hippocampus. For all electrophysiological recordings, extracellular spike signals of either tungsten stereotrodes or Pt recording sites were simultaneously pre-amplified ($20\times$), filtered (band pass, $600\,Hz$–$6\,kHz$) and sampled at $30\,kHz$ using the integrated Digital Lynx recording system (Neuralynx). To evaluate signal quality, the signal-to-noise ratio was defined as the peak-to-valley amplitude of the spikes divided by the s.d. of the noise, and we showed scatter plot of spike peak-to-valley amplitude against signal-to-noise ratio (see tungsten stereotrode recording in Supplementary Fig. 14d and integrated probe recording in Supplementary Fig. 16d), and the spike detection threshold was set as three times of the s.d. of the noise level.

For patterned-light stimulation, we delivered 1 ms laser pulses at multiple frequencies (40 Hz, 80 Hz and 200 Hz) and patterns (regular bursting or random). A pulse generator (Sanworks LLC PulsePal v.2)[57] was programmed using Matlab through a serial interface, which sent seven analogue voltage outputs in different combinations to control the optical switch network and one synchronized transistor–transistor logic output to trigger the laser pulse. The timing for switch voltage and laser pulse were acquired by splitting the transistor–transistor logic output channel to the digital input–output port of the recording system (see Supplementary Fig. 3 for the experimental setup). We screened for neural activity on the basis of an on-line peri-stimulus time histogram (HistogramDisplay v.1.3.0, Neuralynx) by aligning spike events to the onset of each light pulse. In initial experiments, we observed light-induced electrical artefacts, but these were eliminated by (1) blocking the light leakage from the external fibre coupling and (2) placing the tungsten electrode tip out of the cone of light. Supplementary Fig. 7 shows that light-induced artefacts are very tightly time-locked to the light pulse onset, whereas real light-induced spikes have more temporal jitter.

Electrophysiological-data analysis. All data analysis was carried out using built-in and custom-built software in Matlab (Mathworks). We recorded well-isolated single-neuron units and delivered brief (1 ms) blue light pulses to elicit light-induced spikes. Optogenetically tagged neurons were identified by their significant short-latency light response using stimulus-associated spike latency test (SALT) for optical tagging identification[58]. We show examples of spike sorting and statistics of the spike sorting quality in Supplementary Figs. 13–16 using the tungsten stereotrodes and integrated Pt electrodes. These quantitative measures show that our spike-sorting approach offers good cluster quality and reliably identifies well-isolated light-tagged neuron units.

Spike sorting. Spikes were manually sorted into clusters off-line using the MClust software as described from previous literature[59]. For recordings using tungsten stereotrodes, we chose waveform energy and peak amplitude features, which showed the best cluster separation (see Supplementary Figs. 13 and 14). The tungsten stereotrodes comprise two closely spaced recording channels. For recordings using integrated Pt single-electrode configuration, we chose waveform peak and valley amplitude features, which showed the best cluster separation (see Supplementary Figs. 15 and 16). Cluster quality was quantified using isolation distance (ID) and L-ratio[60]. The isolation distance is a measure of how well separated a cluster is from the rest of the data set and L-ratio indicates the distribution of non-cluster spikes around a cluster. A low L-ratio indicates that there is a relatively empty space between the cluster and other spikes in the data set. Therefore, a higher ID and a lower L-ratio together indicate better cluster quality. In this work, we exclude putative neurons with ID < 18 or L-ratio > 0.2 (see Supplementary Figs. 14a–c and 16a–c). Autocorrelation functions were inspected and in cases of absolute refractory period violations, an additional effort was made to improve cluster separation. We excluded the cluster if refractory violations persisted.

Stimulus-associated spike latency test. The directly light-activated neuron was identified based on a statistical test called SALT, which tests the hypothesis that the post-stimulus spike latency distribution after light stimuli is significantly different from a stimulus-free baseline distribution. To measure the distance between these two distributions, we used an information-theory measure (modified Jensen–Shannon divergence), which has been described in detail previously[58]. A cut-off value of $P < 0.01$ is applied to define light-tagged neurons. In this work, the yielded low P value ($P < 0.001$) suggested direct light activated neurons (in blue) as shown in Supplementary Figs. 14e and 16e where P values of light-tagged and non-light-tagged neurons are shown.

Light-induced spikes were defined on the basis of the peak of peri-stimulus time histogram aligned to light stimuli (spikes shown within full width at half-height windows). These spikes were marked in colour on the waveform feature space used for spike sorting (see Supplementary Figs. 13 and 15). For each light-tagged neuron, we showed that the light-induced spikes were overlaid with spontaneous spikes from the same cluster and well separated from other non-light-tagged neuron clusters.

Optical-tagging statistics. To address the issue of spike fidelity, light-induced spike probability was defined as the proportion of successfully light-induced spikes to light pulses. To quantify the light-activation effect, light-induced spike latency was defined as the time from light-pulse onset to the time of the spike that occurred after the onset of a light pulse. Light-induced spike jitter was defined as the standard deviation, across repeated trials, of the timing of the spike that occurred after the onset of a light pulse. To ensure that the spike sorting was not compromised by light application, the waveform similarities of light evoked and spontaneous spike were computed using Pearson's correlation coefficient. Direct light-activated neurons showed similar spontaneous and light-induced waveforms (high spike similarity, r value), high light-induced spike probability, short light-induced spike latency and low light-induced spike jitter.

Histology. Following acute electrophysiology recordings, mice were anaesthetized and transcardially perfused with 0.9% saline followed by 4% paraformaldehyde in PBS. Brains were extracted, immersed in 4% paraformaldehyde for 24 h, and then prepared for sectioning by washing with PBS three times, each wash lasting 5 min. The brain tissue was embedded with 2% agarose gel, mounted on the vibratome stage (Leica VT 1000S) and sliced into 90-μm-thick coronal sections including the V1 and hippocampus. The tungsten stereotrodes were coated with DiI labelling solution (Vybrant) before surgery so that the insertion track could be verified histologically (see Supplementary Fig. 4). The histological images were acquired with a Zeiss LSM780 confocal laser scanning microscope.

Reporting Summary. Further information on research design is available in the Nature Research Reporting Summary linked to this article.

Data availability
The main data supporting the results in this study are available within the paper and its Supplementary Information. The raw and analysed datasets generated during the study are too large to be publicly shared, but they are available for research purposes from the corresponding authors on reasonable request.

Code availability
The code packages MClust 3.5 and CellBase R2013a are openly available at http://redishlab.neuroscience.umn.edu/mclust/MClust.html and https://github.com/hangyabalazs/CellBase.

References
1. Atabaki, A. H. et al. Integrating photonics with silicon nanoelectronics for the next generation of systems on a chip. *Nature* **556**, 349–354 (2018).
2. Xu, Q., Schmidt, B., Pradhan, S. & Lipson, M. Micrometre-scale silicon electro-optic modulator. *Nature* **435**, 325–327 (2005).
3. Reed, G. T., Mashanovich, G., Gardes, F. Y. & Thomson, D. J. Silicon optical modulators. *Nat. Photon.* **4**, 518–526 (2010).
4. Dai, D., Wang, J., Chen, S., Wang, S. & He, S. Monolithically integrated 64-channel silicon hybrid demultiplexer enabling simultaneous wavelength- and mode-division-multiplexing: monolithically integrated 64-channel silicon hybrid demultiplexer. *Laser Photon. Rev.* **9**, 339–344 (2015).
5. Sun, J., Timurdogan, E., Yaacobi, A., Hosseini, E. S. & Watts, M. R. Large-scale nanophotonic phased array. *Nature* **493**, 195–199 (2013).
6. Hutchison, D. N. et al. High-resolution aliasing-free optical beam steering. *Optica* **3**, 887 (2016).
7. Phare, C. T., Shin, M. C., Miller, S. A., Stern, B. & Lipson, M. Silicon optical phased array with high-efficiency beam formation over 180 degree field of view. Preprint at https://arxiv.org/abs/1802.04624 (2018).
8. Shen, Y. et al. Deep learning with coherent nanophotonic circuits. *Nat. Photon.* **11**, 441–446 (2017).
9. Harris, N. C. et al. Quantum transport simulations in a programmable nanophotonic processor. *Nat. Photon.* **11**, 447–452 (2017).
10. Segev, E. et al. Patterned photostimulation via visible-wavelength photonic probes for deep brain optogenetics. *Neurophotonics* **4**, 011002 (2016).
11. Shim, E., Chen, Y., Masmanidis, S. & Li, M. Multisite silicon neural probes with integrated silicon nitride waveguides and gratings for optogenetic applications. *Sci. Rep.* **6**, 22693 (2016).
12. Li, B., Lee, K., Masmanidis, S. C. & Li, M. A nanofabricated optoelectronic probe for manipulating and recording neural dynamics. *J. Neural Eng.* **15**, 046008 (2018).

13. Selvaraja, S. K., Bogaerts, W., Dumon, P., Van Thourhout, D. & Baets, R. Subnanometer linewidth uniformity in silicon nanophotonic waveguide devices using CMOS fabrication technology. *IEEE J. Sel. Top. Quantum Electron.* **16**, 316–324 (2010).

14. Choy, J. T. et al. Integrated TiO_2 resonators for visible photonics. *Opt. Lett.* **37**, 539 (2012).

15. Jun, J. J. et al. Fully integrated silicon probes for high-density recording of neural activity. *Nature* **551**, 232–236 (2017).

16. Du, J., Blanche, T. J., Harrison, R. R., Lester, H. A. & Masmanidis, S. C. Multiplexed, high density electrophysiology with nanofabricated neural probes. *PLoS ONE* **6**, e26204 (2011).

17. Pisanello, F. et al. Dynamic illumination of spatially restricted or large brain volumes via a single tapered optical fiber. *Nat. Neurosci.* **20**, 1180–1188 (2017).

18. Wu, F. et al. Monolithically integrated µLEDs on silicon neural probes for high-resolution optogenetic studies in behaving animals. *Neuron* **88**, 1136–1148 (2015).

19. Kim, T.-I. et al. Injectable, cellular-scale optoelectronics with applications for wireless optogenetics. *Science* **340**, 211–216 (2013).

20. Scharf, R. et al. Depth-specific optogenetic control in vivo with a scalable, high-density µLED neural probe. *Sci. Rep.* **6**, 28381 (2016).

21. Shemesh, O. A. et al. Temporally precise single-cell-resolution optogenetics. *Nat. Neurosci.* **20**, 1796–1806 (2017).

22. Peron, S. & Svoboda, K. From cudgel to scalpel: toward precise neural control with optogenetics. *Nat. Methods* **8**, 30–34 (2011).

23. Yang, Y., DeWeese, M. R., Otazu, G. H. & Zador, A. M. Millisecond-scale differences in neural activity in auditory cortex can drive decisions. *Nat. Neurosci.* **11**, 1262–1263 (2008).

24. deCharms, R. C. & Merzenich, M. M. Primary cortical representation of sounds by the coordination of action-potential timing. *Nature* **381**, 610–613 (1996).

25. Hahnloser, R. H. R., Kozhevnikov, A. A. & Fee, M. S. An ultra-sparse code underlies the generation of neural sequences in a songbird. *Nature* **419**, 65–70 (2002).

26. Watts, M. R. et al. Adiabatic thermo-optic Mach–Zehnder switch. *Opt. Lett.* **38**, 733–735 (2013).

27. Cai, X. et al. Integrated compact optical vortex beam emitters. *Science* **338**, 363–366 (2012).

28. Ji, N., Freeman, J. & Smith, S. L. Technologies for imaging neural activity in large volumes. *Nat. Neurosci.* **19**, 1154–1164 (2016).

29. Tanizawa, K. et al. Ultra-compact 32×32 strictly-non-blocking Si-wire optical switch with fan-out LGA interposer. *Opt. Express* **23**, 17599 (2015).

30. Phare, C. T., Daniel Lee, Y.-H., Cardenas, J. & Lipson, M. Graphene electro-optic modulator with 30 GHz bandwidth. *Nat. Photon.* **9**, 511–514 (2015).

31. Poulton, C. V. et al. Coherent solid-state LIDAR with silicon photonic optical phased arrays. *Opt. Lett.* **42**, 4091 (2017).

32. Zhang, F. et al. The microbial opsin family of optogenetic tools. *Cell* **147**, 1446–1457 (2011).

33. Zortman, W. A., Trotter, D. C. & Watts, M. R. Silicon photonics manufacturing. *Opt. Express* **18**, 23598–23607 (2010).

34. Wagner, H., Brill, S., Kempter, R. & Carr, C. E. Microsecond precision of phase delay in the auditory system of the barn owl. *J. Neurophysiol.* **94**, 1655–1658 (2005).

35. Garcia-Lazaro, J. A., Belliveau, L. A. C. & Lesica, N. A. Independent population coding of speech with sub-millisecond precision. *J. Neurosci.* **33**, 19362–19372 (2013).

36. Bale, M. R., Campagner, D., Erskine, A. & Petersen, R. S. Microsecond-scale timing precision in rodent trigeminal primary afferents. *J. Neurosci.* **35**, 5935–5940 (2015).

37. Boyden, E. S., Zhang, F., Bamberg, E., Nagel, G. & Deisseroth, K. Millisecond-timescale, genetically targeted optical control of neural activity. *Nat. Neurosci.* **8**, 1263–1268 (2005).

38. Hoffman, L. et al. High-density optrode-electrode neural probe using SixNy photonics for in vivo optogenetics. In *IEEE International Electron Devices Meeting* (ed. Suehle, J.) 29.5.1–29.5.4. (IEEE, 2015).

39. Zorzos, A. N., Scholvin, J., Boyden, E. S. & Fonstad, C. G. Three-dimensional multiwaveguide probe array for light delivery to distributed brain circuits. *Opt. Lett.* **37**, 4841–4843 (2012).

40. Zorzos, A. N., Boyden, E. S. & Fonstad, C. G. Multiwaveguide implantable probe for light delivery to sets of distributed brain targets. *Opt. Lett.* **35**, 4133–4135 (2010).

41. Schwaerzle, M., Paul, O. & Ruther, P. Compact silicon-based optrode with integrated laser diode chips, SU-8 waveguides and platinum electrodes for optogenetic applications. *J. Micromech. Microeng.* **27**, 065004 (2017).

42. Ji, X. et al. Ultra-low-loss on-chip resonators with sub-milliwatt parametric oscillation threshold. *Optica* **4**, 619–624 (2017).

43. Thomson, D. J., Hu, Y., Reed, G. T. & Fedeli, J.-M. Low loss MMI couplers for high performance MZI modulators. *IEEE Photonics Technol. Lett.* **22**, 1485–1487 (2010).

44. Mikkelsen, J. C., Sacher, W. D. & Poon, J. K. S. Dimensional variation tolerant silicon-on-insulator directional couplers. *Opt. Express* **22**, 3145–3150 (2014).

45. Gunaydin, L. A. et al. Ultrafast optogenetic control. *Nat. Neurosci.* **13**, 387–392 (2010).

46. Densmore, A. et al. Compact and low power thermo-optic switch using folded silicon waveguides. *Opt. Express* **17**, 10457–10465 (2009).

47. Fang, Q. et al. Ultralow power silicon photonics thermo-optic switch with suspended phase arms. *IEEE Photonics Technol. Lett.* **23**, 525–527 (2011).

48. Maese-Novo, A. et al. Wavelength independent multimode interference coupler. *Opt. Express* **21**, 7033–7040 (2013).

49. Chen, X., Li, C., Fung, C. K. Y., Lo, S. M. G. & Tsang, H. K. Apodized waveguide grating couplers for efficient coupling to optical fibers. *IEEE Photonics Technol. Lett.* **22**, 1156–1158 (2010).

50. Horton, N. G. et al. In vivo three-photon microscopy of subcortical structures within an intact mouse brain. *Nat. Photon.* **7**, 205–209 (2013).

51. Karpov, M., Pfeiffer, M. H. P., Liu, J., Lukashchuk, A. & Kippenberg, T. J. Photonic chip-based soliton frequency combs covering the biological imaging window. *Nat. Commun.* **9**, 1146 (2018).

52. Halir, R. et al. Ultrabroadband supercontinuum generation in a CMOS-compatible platform. *Opt. Lett.* **37**, 1685–1687 (2012).

53. Zhao, H. et al. Visible-to-near-infrared octave spanning supercontinuum generation in a silicon nitride waveguide. *Opt. Lett.* **40**, 2177–2180 (2015).

54. Ikeda, K., Saperstein, R. E., Alic, N. & Fainman, Y. Thermal and Kerr nonlinear properties of plasma-deposited silicon nitride/silicon dioxide waveguides. *Opt. Express* **16**, 12987–12994 (2008).

55. Ahrens, M. B., Orger, M. B., Robson, D. N., Li, J. M. & Keller, P. J. Whole-brain functional imaging at cellular resolution using light-sheet microscopy. *Nat. Methods* **10**, 413–420 (2013).

56. Pégard, N. C. et al. Compressive light-field microscopy for 3D neural activity recording. *Optica* **3**, 517–524 (2016).

57. Sanders, J. I. & Kepecs, A. A low-cost programmable pulse generator for physiology and behavior. *Front. Neuroeng.* **7**, 43 (2014).

58. Kvitsiani, D. et al. Distinct behavioural and network correlates of two interneuron types in prefrontal cortex. *Nature* **498**, 363–366 (2013).

59. Pi, H.-J. et al. Cortical interneurons that specialize in disinhibitory control. *Nature* **503**, 521–524 (2013).

60. Schmitzer-Torbert, N., Jackson, J., Henze, D., Harris, K. & Redish, A. D. Quantitative measures of cluster quality for use in extracellular recordings. *Neuroscience* **131**, 1–11 (2005).

Acknowledgements

Author contributions

A.M. designed and tested the performance of the nanophotonic probe. Q.L. performed the animal surgery, histological analysis and electrophysiology data analysis. A.M. and Q.L. developed and conducted the in vivo electrophysiology experiment with the assistance of M.A.T. and S.P.R. A.M. fabricated the nanophotonic probe with the assistance of X.J. and J.C. S.P.R. developed and fabricated the integrated recording electrode process. E.S. and G.R.B. assisted with back-end fabrication processing and electrical packaging, respectively. A.M. and M.A.T. developed the fibre packaging for in vivo experiments. S.A.M. developed the software interface for optical characterization. A.M., Q.L., M.A.T., A.K. and M.L. designed the experiment and discussed the results. A.M., Q.L. and M.A.T. designed and built the experimental setup. A.K. and M.L. supervised the project. A.M., Q.L., A.K. and M.L. prepared the manuscript. M.A.T., S.P.R., G.R.B., E.S., X.J., J.C. and S.A.M. edited the manuscript.

Competing interests

A.M., Q.L., M.A.T., X.J., A.K. and M.L. are listed as inventors in a patent application related to this work, filed by Columbia University. The remaining authors declare no competing interests.

Additional information

Supplementary information is available for this paper at https://doi.org/10.1038/s41551-020-0516-y.

Correspondence and requests for materials should be addressed to A.K. or M.L.

Reprints and permissions information is available at www.nature.com/reprints.

Publisher's note Springer Nature remains neutral with regard to jurisdictional claims in published maps and institutional affiliations.

Corresponding author(s):   Michal Lipson, Adam Kepecs

Last updated by author(s): Dec 19, 2019

Reporting Summary

Nature Research wishes to improve the reproducibility of the work that we publish. This form provides structure for consistency and transparency in reporting. For further information on Nature Research policies, see Authors & Referees and the Editorial Policy Checklist.

Statistics

For all statistical analyses, confirm that the following items are present in the figure legend, table legend, main text, or Methods section.

n/a	Confirmed	
☐	☒	The exact sample size (*n*) for each experimental group/condition, given as a discrete number and unit of measurement
☐	☒	A statement on whether measurements were taken from distinct samples or whether the same sample was measured repeatedly
☐	☒	The statistical test(s) used AND whether they are one- or two-sided *Only common tests should be described solely by name; describe more complex techniques in the Methods section.*
☒	☐	A description of all covariates tested
☒	☐	A description of any assumptions or corrections, such as tests of normality and adjustment for multiple comparisons
☐	☒	A full description of the statistical parameters including central tendency (e.g. means) or other basic estimates (e.g. regression coefficient) AND variation (e.g. standard deviation) or associated estimates of uncertainty (e.g. confidence intervals)
☒	☐	For null hypothesis testing, the test statistic (e.g. *F*, *t*, *r*) with confidence intervals, effect sizes, degrees of freedom and *P* value noted *Give P values as exact values whenever suitable.*
☒	☐	For Bayesian analysis, information on the choice of priors and Markov chain Monte Carlo settings
☒	☐	For hierarchical and complex designs, identification of the appropriate level for tests and full reporting of outcomes
☒	☐	Estimates of effect sizes (e.g. Cohen's *d*, Pearson's *r*), indicating how they were calculated

Our web collection on statistics for biologists contains articles on many of the points above.

Software and code

Policy information about availability of computer code

Data collection	Digital Lynx recording system Cheetah 5.7.4 (Neuralynx, Inc), Histogram Version: 1.3.0 (Neuralynx, Inc), Pulse Pal v2 (open source pulse train generator, Sanworks LLC).
Data analysis	MClust 3.5 (http://redishlab.neuroscience.umn.edu/mclust/MClust.html), and CellBase R2013a (https://github.com/hangyabalazs/CellBase).

For manuscripts utilizing custom algorithms or software that are central to the research but not yet described in published literature, software must be made available to editors/reviewers. We strongly encourage code deposition in a community repository (e.g. GitHub). See the Nature Research guidelines for submitting code & software for further information.

Data

Policy information about availability of data

All manuscripts must include a data availability statement. This statement should provide the following information, where applicable:

- Accession codes, unique identifiers, or web links for publicly available datasets
- A list of figures that have associated raw data
- A description of any restrictions on data availability

The main data supporting the results in this study are available within the paper and its Supplementary Information. The raw and analysed datasets generated during the study are too big to be publicly shared, yet they are available for research purposes from the corresponding authors on reasonable request.

Field-specific reporting

Please select the one below that is the best fit for your research. If you are not sure, read the appropriate sections before making your selection.

☒ Life sciences ☐ Behavioural & social sciences ☐ Ecological, evolutionary & environmental sciences

For a reference copy of the document with all sections, see nature.com/documents/nr-reporting-summary-flat.pdf

Life sciences study design

All studies must disclose on these points even when the disclosure is negative.

Sample size	No statistical methods were used to predetermine sample sizes. Sample sizes were determined on the basis of the authors' experience of what is necessary to generate a convincing and compelling result, and they are in general comparable to sample sizes employed in the field. For the in vivo demonstration, the number of mice was dependent on the yield of usable mice, defined as those in which a field of ChETA well-expressing neurons was obtained and robust neural activities were recorded. For the statistical data shown in Fig. 4e,f and Supplementary Fig. 5c, we included 13 light-tagged Gad2 interneurons' activity data across 4 mice; for the statistical data shown in Supplementary Fig. 7c, we included 13 light-tagged Gad2 interneurons' activity data and 7 light-induced artifacts data across 4 mice; for the statistical data shown in Supplementary Fig. 14, we included 13 light-tagged Gad2 interneurons (blue) and 85 non-light-tagged neurons (grey) from 10 recording sessions of 4 mice; for the statistical data shown in Supplementary Fig. 16, we included 6 light-tagged Gad2 interneurons (blue) and 40 non-light-tagged neurons (grey) from 5 recording sessions of 3 mice.
Data exclusions	Animals were excluded from the study if viral expression was weak, or if no light induced spikes were detected at the recording site during the in vivo experiments.
Replication	We were able to reproduce robust and reliable light-induced spikes with high-efficiency spiking signals across different mice.
Randomization	As a general rule, mice were randomly distributed in each of the cages ordered from the Jackson Laboratory. On arrival, the animals were randomly assigned to the experiments.
Blinding	No blinding was done in this study. Virtually all the data were quantitative, and most measurements were based on neural responses and thus not easily subject to operator bias.

Reporting for specific materials, systems and methods

We require information from authors about some types of materials, experimental systems and methods used in many studies. Here, indicate whether each material, system or method listed is relevant to your study. If you are not sure if a list item applies to your research, read the appropriate section before selecting a response.

Materials & experimental systems

n/a	Involved in the study
☒	☐ Antibodies
☒	☐ Eukaryotic cell lines
☒	☐ Palaeontology
☐	☒ Animals and other organisms
☒	☐ Human research participants
☒	☐ Clinical data

Methods

n/a	Involved in the study
☒	☐ ChIP-seq
☒	☐ Flow cytometry
☒	☐ MRI-based neuroimaging

Animals and other organisms

Policy information about studies involving animals; ARRIVE guidelines recommended for reporting animal research

Laboratory animals	Gad2-IRES-Cre knock-in mice (Jackson Laboratory Stock No. 010802), adult (6–8 months old) male or female (~25 g).
Wild animals	The study did not involve wild animals.
Field-collected samples	The study did not involve samples collected from the field.
Ethics oversight	All procedures involving animals were carried out in accordance with the protocol approved by Cold Spring Harbor Laboratory Institutional Animal Care and Use Committee, in accordance with National Institutes of Health regulations.

Note that full information on the approval of the study protocol must also be provided in the manuscript.